

# Twisting Linear to Orbital Angular Momentum in an Ultrasonic Motor

Jingjing Liu, Zhengwei Li, Yujiang Ding, An Chen, Bin Liang,\* Jing Yang, Jian-Chun Cheng,\* and Johan Christensen\*

An ultrasonic motor built with a contactless meta engine block (MEB) is designed and experimentally demonstrated for twisting the linear momentum of sound emanating from a Helmholtz resonator-based metasurface into orbital angular momentum (OAM). The MEB is capable of hosting highly efficient excitations of eigenmodes carrying desired OAM whose Bessel acoustic intensity patterns are enhanced by over ten times compared to the incident wave. Thanks to this efficiency, bidirectional ultrasonic OAM is capable of driving loads at speeds up to 1000 rpm at 4 W and remarkable sound radiation torque levels. Moreover, the possibility of using arbitrarily shaped MEBs is also demonstrated by engineering its physical boundary condition based on an analytically derived criterion to guarantee the high twisting efficiency of man-made OAM. The results show how noninvasive driving of an ultrasonic motor can be made possible through appropriately designed momentum twisting, which opens the door to a new class of integrated mechanical devices solely powered by sound.

sound vortices with engineered topological charges, which are motivated by their ability to achieve specific wave fields to acquire three-dimensional (3D) trapping and translation of particles and to flexibly transfer OAM.<sup>[12–21]</sup>

Beyond the current state-of-the-art technologies comprising the 3D sonic maneuvering,<sup>[22]</sup> levitation, and manipulation of particles,<sup>[23]</sup> it is also highly appealing to enable precision rotation of particles, i.e., steady and controllable rotary motion without a piston, combustion or magnetic fields. This avenue would call for an acoustic motor driven by OAM-induced acoustic radiation torque to actuate micromachines, or allow controllable rotation of tiny objects in a contactless and flexible way. Thus, how to efficiently and simply introduce OAM, as a power source, in an acoustic motor, is pivotal for its practical implementation.

Vortex beams propagating in 3D space with spiral wavefront spreading infinitely along propagation direction usually require an external input beam that originates from a separate sound source,<sup>[24–27]</sup> which results in a bottleneck for the integration and miniaturization of the acoustically actuated motor. On the other hand, in-plane production of OAM offers a more compact and robust solution to obtain highly pure coherent vortex modes. However, this usually relies on numerous axisymmetrically placed bulky sources,<sup>[28–30]</sup> tailored energy gain/loss in a parity-time symmetric ring cavity<sup>[31–33]</sup> or whispering gallery modes in microcavities with low coupling efficiency,<sup>[34]</sup> except for the topological vortex states between neighboring unit cells in periodic systems with large dimension.<sup>[35]</sup> In addition to the increased implementation complexity and energy loss, how to apply such acoustic motor in real-world systems with compact design or irregular geometry still remains challenging if not impossible.

Here, we propose a compact ultrasonic motor based on the conversion of linear to angular momentum in its meta engine block (MEB), with no restrictions on source number, geometric shape, or nonhermicity of the system. The mechanism is to rationally design the MEB's boundary condition based on an analytically derived criterion such that high-efficiency excitation of eigenmode carrying desired OAM can be achieved. Furthermore, the excited mode with a symmetrical pattern extends to fill the whole region inside the MEB despite its irregularity and compactness. We demonstrate the performance of the designed

## 1. Introduction

The use of acoustic forces to manipulate or trap objects is an emerging field that has sparked tremendous interest among scientists and engineers in biology, chemistry, and medicine.<sup>[1–4]</sup> Noninvasively to be able to handle both in space and time small objects, such as cells and organisms, play a central role in the above areas based on the horizon of possibilities offered by the contact-free and biocompatible means of maneuvering and controlling of objects.<sup>[5–11]</sup> Recent efforts have focused on

J. Liu, Z. Li, Y. Ding, A. Chen, B. Liang, J. Yang, J.-C. Cheng  
Collaborative Innovation Center of Advanced Microstructures  
and Key Laboratory of Modern Acoustics  
MOE

Institute of Acoustics  
Department of Physics  
Nanjing University  
Nanjing 210093, China  
E-mail: liangbin@nju.edu.cn; jccheng@nju.edu.cn

J. Christensen  
Department of Physics  
Universidad Carlos III de Madrid  
Leganés, Madrid ES-28916, Spain  
E-mail: johan.christensen@uc3m.es

 The ORCID identification number(s) for the author(s) of this article can be found under <https://doi.org/10.1002/adma.202201575>.

DOI: 10.1002/adma.202201575

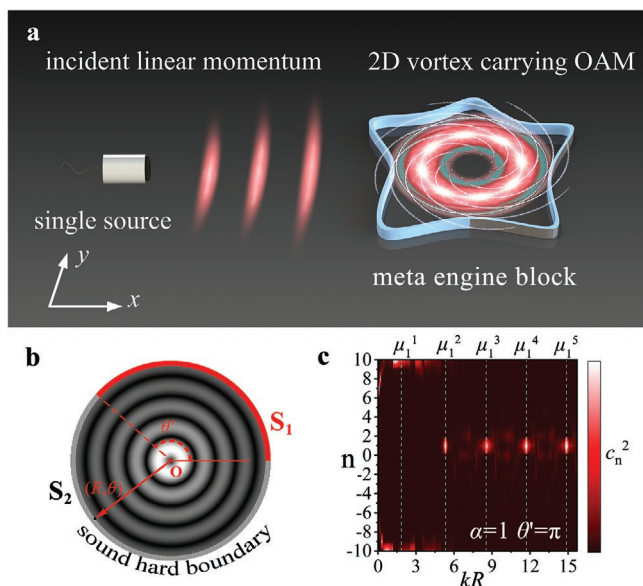


**Figure 1.** Ultrasonic motor for momentum twisting. a) Schematic of proposed compact and arbitrarily shaped MEB for twisting linear wavevector of the incident plane wave to in-plane OAM-carrying vortex with its boundary judiciously modulated according to the initial geometry and the target OAM. b) Definition of coordinate system and boundary condition used for generating OAM in an axisymmetric MEB. c) Mode distribution of  $c_n^2$  versus radius  $R$  and mode index  $n$  for a particular boundary condition.

acoustic motor via numerical simulations and experimental measurements, including contactless driving of loads to rotate clockwise or counterclockwise with a speed up to 1000 rpm at 25 kHz and producing a 2D vortex beam of desired order within a fan-shaped region at audio frequency.

## 2. Results and Discussion

### 2.1. Working Mechanism of the Ultrasonic Motor

**Figure 1a** schematically illustrates our proposed ultrasonic motor as a compact and planar device built by an arbitrarily shaped MEB, which in 2D wave systems behaves as a cavity with customizable boundary condition, enabling a new mechanism of twisting linear momentum (emitted from a single source) to OAM by modulating the device's boundary. Intrinsically, in free space the wave emitted from a single source contains no desired OAM given the conservation of angular momentum. Hence, our mechanism modulates parts of the boundary to be totally reflective to provide a counter-propagating wavevector opposite to the incident wave (gray part in **Figure 1a**), which is essential for the existence of a couple of torsional momenta. However, the wave field excited in this MEB should be composed of multiple eigenmodes, and moreover, will become extremely complicated for more general cases where the MEB has an irregular geometry, as will be discussed later. A simple and precise production of a 2D vortex field carrying a specific order of OAM thus becomes highly challenging. To this end, we begin with a simplest case where the MEB is perfectly

circular, and analytically prove the possibility of solving this difficulty by rationally engineering its physical boundary condition. According to the conservation law, for generating the OAM in this axisymmetric MEB, the remaining part of the boundary must have a spiral angular dependence of phase, in combination with the reflective part. Hence, the boundary condition is expressed as follows:

$$p(\theta) = p_0 e^{i\alpha\theta} (\theta \in S_1), \frac{\partial p}{\partial n} \Big|_{r=R} = 0 (\theta \in S_2) \quad (1)$$

where  $S_1$  and  $S_2$  refer to the spiral phase and reflective boundary respectively (**Figure 1b**). For a Helmholtz equation in cylindrical coordinates, the general solution can be expressed as a sum of cylindrical Bessel modes:

$$p(r, \theta) = \sum_n A_n J_n(kr) e^{in\theta} \quad (2)$$

where  $J_n(kr)$  is an  $n$ th-order Bessel function of the first kind with  $k$  being the wave number and  $A_n$  is the corresponding modal amplitude. The uniqueness theorem implies that the wave field inside this 2D symmetrical region can be solved by substituting Equation (2) into Equation (1). Then we derive the critical criterion ( $kR = \mu_n^i$ ) for precise excitation of the target eigenmode carrying  $m$ th-order OAM in such a system, where  $\mu_n^i$  are the zeros of the derivative of the  $m$ th-order Bessel function; see the entire derivation in Supporting Information.

For quantitatively evaluating the relative amplitude of each mode, we introduce a parameter of normalized mode coefficient, defined as:

$$c_n = \frac{|A_n|}{\sum_{n=-M}^M |A_n|} \quad (3)$$

**Figure 1c** shows the analytical results of  $c_n^2$  versus  $R$  and  $n$  for a typical MEB. The results reveal a series of discrete maxima of  $c_1^2$  appearing at specific points  $\mu_1^i$ , indicating the introduction of desired 1st-order OAM by judiciously adjusting the boundary condition to meet the derived criterion. It is also obvious that our designed MEB generally applies to the production of OAM with any other topological charges in the same manner (**Figure S2**, Supporting Information). Notice that the reduction of the MEB's radius may induce the production of some high-order OAMs yet do not contribute to the resulting sound field inside the MEB due to the huge null-pressure center regions of these modes. Here, we introduce a passive reflective boundary that can be easily implemented with natural materials. As a result, our proposed mechanism breaks with the dependence on circularly arranged bulky source arrays, yet enables transverse OAM generation in a single artificial cavity irradiated by a single source, with practical significance in terms of simplification and integration of on-chip OAM devices.

The above derivation is based on the pressure-driven boundary condition for which the pressure  $p$  at the MEB's boundary is given, yet our methodology also opens a new route to the OAM production with active devices that usually are velocity-driven.<sup>[28,29]</sup> This approach facilitates significantly reduced system complexity and allows the application in more complex environments. The requirement for introducing

$m$ th-order OAM under this circumstance can be deduced as (see Supporting Information):

$$kR = \mu_m^i (\alpha + m) \theta' = 2l\pi \quad (4)$$

where  $l$  is a nonzero integer. We also analytically calculate the field distribution generated inside the MEB under the sound pressure and velocity excitations of our modulated boundary conditions as illustrated in **Figure 2a,b**. The results for these four particular cases reveal that our acoustic motor using MEB can efficiently and precisely produce the OAM of desired order, regardless of the boundary of the target axisymmetric region.

## 2.2. Arbitrarily Shaped MEB

We move now to more general cases where the MEB may have an arbitrary geometrical shape without azimuthal symmetry for which the above theory cannot directly apply. The complexity of the excited eigenstates in such a cavity will increase dramatically due to the lack of geometrical symmetry as mentioned above. Next, we will demonstrate how to establish an equivalence between the physical boundary and a virtual boundary with perfect azimuthal symmetry and, based on this, generalizing the formula derived above to predict the boundary condition for the production of the desired order of OAM. An arbitrarily shaped physical boundary can be mapped to a virtual circular boundary with a radius of  $kR = \mu_m^i$  by compensating with an additional phase  $\Delta\Phi_m^i = k(r - \mu_m^i)$ , as depicted in **Figure 2c**. Hence, for a MEB  $S(r, \theta)$  of any arbitrary shape, the generalized formula of the boundary condition for generating an  $m$ th-order OAM can

be derived by superposing the spiral phase with an additional compensation phase, as follows:

$$\Phi(r, \theta) = \begin{cases} m\theta + k\left(r - \frac{\mu_m^i}{k}\right), & 0 < \theta < \theta' \\ k\left(r - \frac{\mu_m^i}{k}\right), & \theta' \leq \theta < 2\pi \end{cases} \quad (5)$$

where the phase profile at the boundary can be provided by modulating the structural parameter for different metastructure unit cells.<sup>[36–39]</sup> Performances of our methodology are demonstrated via numerical simulation first. Throughout the paper, the finite element method based on COMSOL Multiphysics software is used for the numerical simulations. As a typical example, we consider the excitation of a 1st-order vortex in an irregular MEB of pentagram shape. By designing part of the boundary as reflective and modulating the phase profile following Equation (5), a vortex that carries the desired OAM and extends the whole pentagram MEB is excited with an external plane wave as numerically illustrated in **Figure 2d** (see Supporting Information for details). The numerical result clearly shows a virtual suppression of all the other modes that would otherwise co-exist in such an irregularly shaped cavity.

The proposed mechanism also applies to the underwater environment by using a soft reflective boundary, which would be of fundamental interest in many important scenarios such as underwater communication or acoustic camouflage.<sup>[40,41]</sup> More importantly, since all the above derivations are based on the solution of the Helmholtz equation, our strategy is general for 2D classical wave systems and offers an alternative method

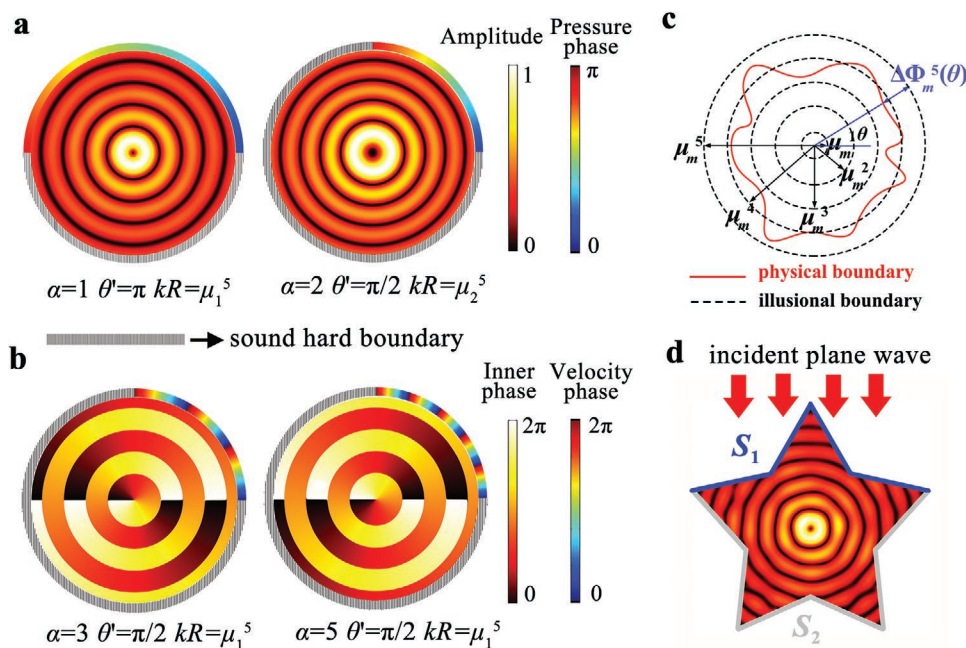


**Figure 2.** The excitations of eigenmodes carrying target OAM inside MEBs. a) Normalized acoustic pressure distributions with two aimed order  $m = 1, 2$  inside MEBs under pressure-driven boundary conditions. b) Phase distributions with target orders  $m = +1, -1$  inside MEBs under velocity-driven boundary conditions. c) Schematic diagram of the virtual transformation from irregular physical boundary (red line) to illusional circular boundary (black lines) by a compensation phase  $\Delta\Phi_m^i$ . d) Simulated normalized acoustic pressure distribution inside a pentagram MEB with boundary condition modulated according to Equation (5).

to introducing OAM such as for 2D acoustic bulk wave systems,<sup>[42]</sup> surface acoustic wave devices,<sup>[43]</sup> spoof surface acoustic wave systems,<sup>[30,44]</sup> surface plasmon polariton systems,<sup>[45]</sup> etc. In addition, despite that the excited in-plane OAMs are the eigenmodes of the MEB cavity and cannot propagate out of the plane, our system can in principle be extended to enable mode conversion from a 2D vortex inside the cavity to a 3D vortex beam propagating in free space.

### 2.3. Experimental Realization of High-Efficient Momentum Twisting Using Ultrasonic Motor

To demonstrate the generality of our mechanism, here the MEB is designed to have a three-quarter-circular rigid boundary while the rest is set to be a straight line (marked by  $S_1$  in Figure 3a), such that the whole boundary is lacking any azimuthal symmetry. The working frequency is set to 25 kHz, for which the sound radiation force is high enough to drive the loads. The designed MEB is placed in a 2D waveguide with sound-absorbing foam mounted at the boundary and three parallel transducers emitting linear momentum, as shown in Figure 3a. In our current experiments, the top of the designed MEB is open to provide a glimpse into the interior. In practical applications, we can easily seal the top of the MEB without affecting the acoustic functionality in a negative way. For simplicity

without losing generality, we demonstrate the production of a 4th-order vortex with radius  $kR = \mu_4^2$ . According to the initial geometric shape and the target OAM, the ideal continuous phase profile on the boundary  $S_1$  can be analytically calculated by Equation (5) with no need of applying an additional phase on the circular parts. As a practical implementation of our strategy, here we choose to design a metastructure unit cell composed of one row of acoustic Helmholtz resonators mounted on a straight channel as illustrated in Figure 3b. In such a design, strong interaction between the incident wave and resonators introduces a large yet controllable phase delay to the transmitted wave, and the straight pipe helps to reduce the impedance mismatch. By judiciously adjusting a single structural parameter  $h$ , one can produce a coupled resonance between them that freely modulates the propagation phase within the full  $2\pi$  range, while keeping high transmission efficiency despite the presence of thermoviscous dissipation. This enables modulating the local boundary condition within a subwavelength physical dimension as demanded in our mechanism (see Figure 3c). Eight building blocks are assembled linearly to implement the boundary  $S_1$  of the MEB and the rest part is acoustically rigid boundary. Hence, for the generation of 4th-order OAM, the discrete phase shift provided by each designed unit as well as its corresponding structural parameter, can be determined and the typical results are depicted in Figure 3d. Figure 3e,f shows the simulated spatial distributions

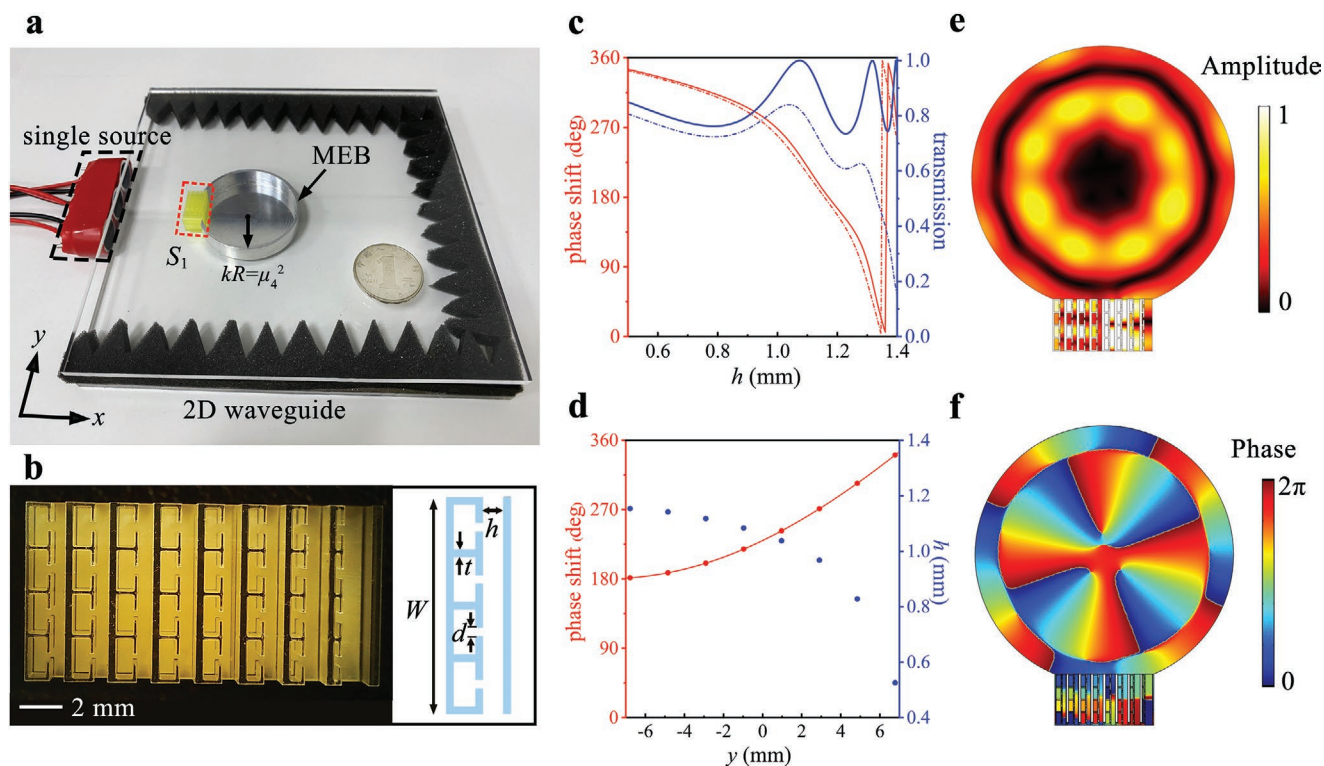


**Figure 3.** Experimental realization of man-made OAM using designed ultrasonic motor. a) Photograph of the experimental setup for twisting linear momentum to 4th-order OAM with designed MEB for ultrasonic frequency of 25 kHz. The dimension of the 2D waveguide is  $15 \times 15 \text{ cm}^2$ . b) Microscopy image of fabricated sample. Inset: 2D cross-section view of an individual unit cell with  $W = 8 \text{ mm}$ ,  $d = 0.4 \text{ mm}$ , and  $t = 0.2 \text{ mm}$ , respectively. c) Simulated phase shift and transmission provided by unit cells versus structural parameter  $h$  with (dashed lines) and without (solid lines) dissipation. d) Continuous phase shift (red line) calculated by Equation (5) and practical discrete phase shift (red dots) provided by unit cells with parameter  $h$  marked by blue dots. e) Simulated sound pressure amplitude and f) phase distribution inside designed MEB.

of the acoustic pressure amplitude and phase of the generated vortex field. The target OAM of the fourth order is precisely generated with the key features of the null center and azimuthal dependence of the phase. Besides, the generated Bessel pattern extends the whole enclosure with the maximum sound intensity reaching up to ten times higher than that of the incident wave, which reveals the high efficiency of OAM conversion by our MEB. It is also noteworthy that the MEB's radius is only 2 cm (1.45 wavelength) and its boundary features deep-subwavelength thickness thanks to the employment of the metastructure, exhibiting the advantage over traditional active devices in terms of significantly downscaled size.

In the following, we will experimentally demonstrate that the designed compact MEB can easily drive sound-absorbing objects within it at remarkably high speed. The physical picture of setting a steady rotation in motion comes from the equilibrium of the viscous torque from the host fluid and the radiation torque exerted by the OAM, which is imprinted by the 2D vortex. We first select a foam disk with a thickness of 2 mm and a diameter of 20 mm as the target object. Initially, the disk is statically aligned at the center of the MEB by a fixed needle. When the single source with a power of 2.5 W is turned on, the foam disk inside the MEB is driven by the radiation torque from the 4th-order OAM and immediately rotates clockwise, after which it quickly reaches a steady state (see Video S1, Supporting Information). Next, we change the operation to generate -4th-order OAM using our MEB by directly flipping its

metastructure array (i.e., boundary  $S_1$ ) and using it to drive the target disk. In such case, the foam disk rotates in an inverse direction with nearly identical speed, as expected. We take five snapshots of the above two rotation processes at the same time interval of 1/60 s, as shown in **Figure 4a,b**. To further exhibit the flexible rotation of tiny objects with different shapes, we use a small foam ball with a radius of 1mm as the load and its orbital motion around the inner wall of the MEB is recorded in **Figure 4c,d** with a time interval of 3/60 s (see Video S2, Supporting Information). The realization of contactless steady rotation of two loads shows clearly the mechanical evidence of OAM transfer. Notice that the load size and shape influence not only the performance of the torque output but also the loads' motional behavior, which can be customized for specific needs in practical applications. For comparison, another control experiment is demonstrated to inspect the load motion in the MEB without the use of the metastructure array whose result is shown in Video S3 (Supporting Information). The result shows that both the foam disk and the small ball do not rotate when the metastructure is absent. In such cases, the MEB excites not only a targeted 4th-order OAM mode but another -4th-order OAM with the same strength, and their superposition generates a near-zero acoustic radiation torque hindering the rotation of the loads. Next, we also quantitatively evaluate the mechanical characteristic of the fabricated ultrasonic motor. We experimentally measure the actual torque output of the disk versus power based on the torque balance and numerically calculate

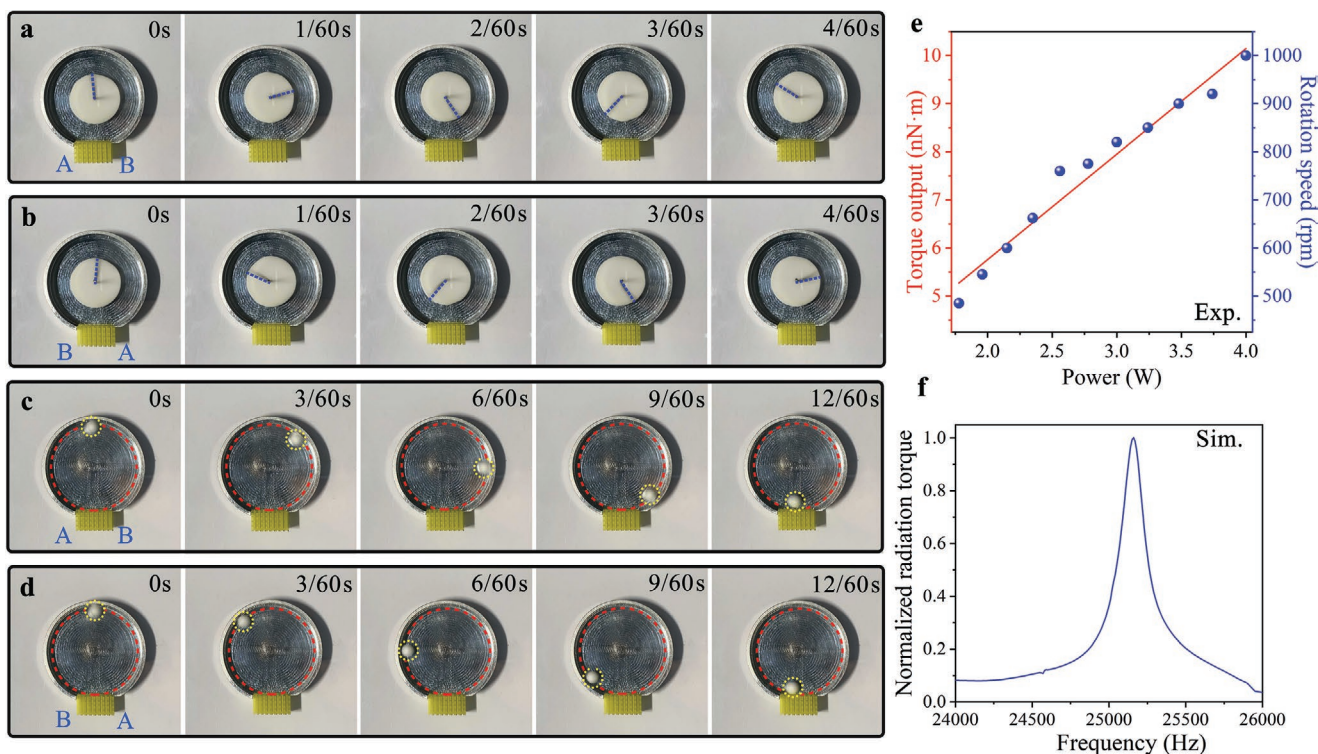


**Figure 4.** Mechanical characteristics of the ultrasonic motor. a,b) Clockwise and anticlockwise rotation of a foam disk using 4th-order (a) and -4th-order (b) 2D vortex beam produced by the MEB. The five snapshots are sequentially captured at the same time interval of 1/60 s. c,d) Orbital motion of a small ball using 4th-order (c) and -4th-order vortex beam (d) produced by the MEB. The time interval of sequencing images is 3/60 s. The orbit is denoted by red dashed line and the small ball is highlighted with a yellow circle. e) Measured rotation speed (blue dots) and actual torque output (red line) of foam disk versus power. f) Simulated acoustic radiation torque versus working frequency.

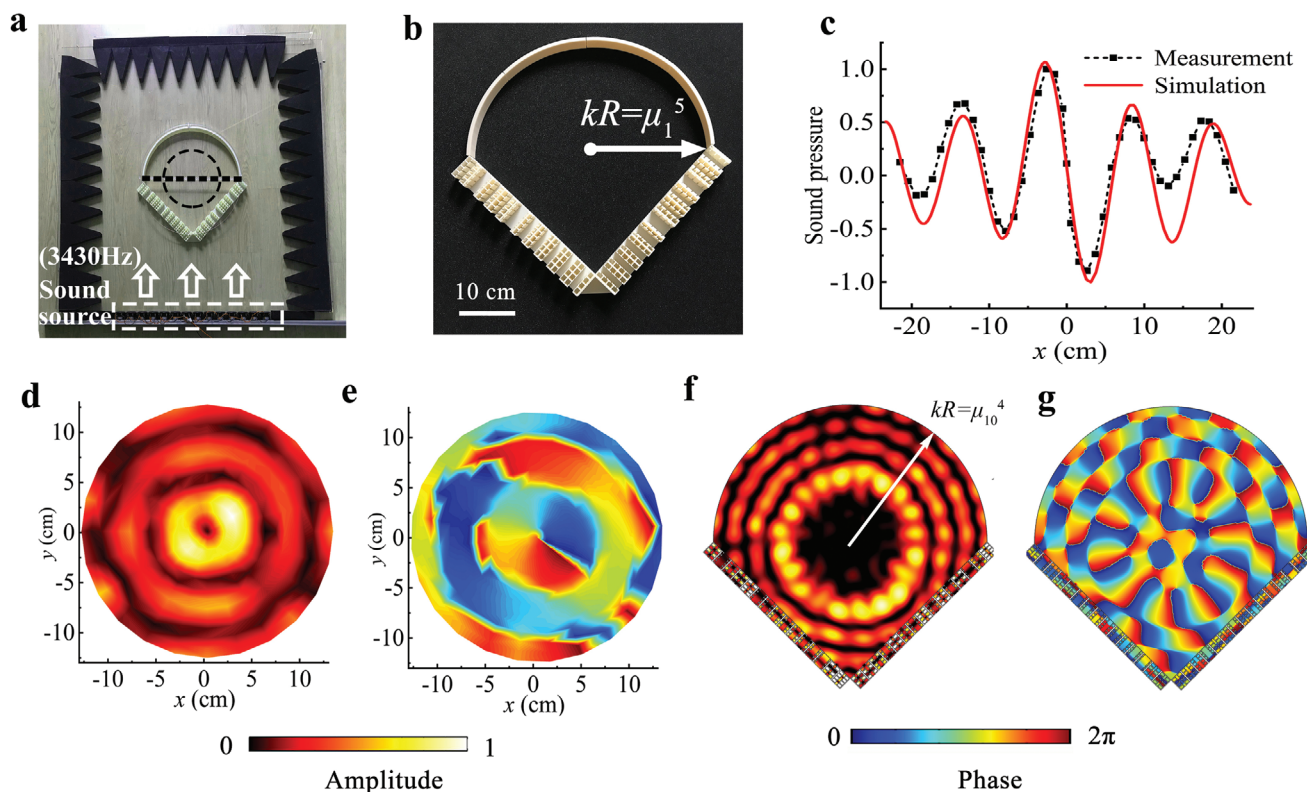


**Figure 5.** Production of man-made OAM using a fan-shaped MEB. a) Photograph of the experimental setup for generating 1st-order OAM within a fan-shaped MEB at audio frequency 3430 Hz. b) Photograph of the fabricated samples of designed MEB consisting of 40 metastructure unit cells and a half-circular solid with a 7.5 mm thickness. c) The measured sound pressure distribution on the axis (black straight line in a) is compared with numerical simulation. d) 2D measured sound relative amplitude and e) phase distribution in circle region with a 13 cm radius (black round line in a). f) Simulated sound pressure amplitude and g) phase distribution inside the MEB with radius  $kR = \mu_{10}^4$  for generating 10th-order OAM.

the acoustic radiation torque in response to the working frequency. In the experiments, when the spinning disk reaches a steady state, the torque output ( $\Gamma_{\text{output}}$ ) produced by the motor and the viscous torque ( $\Gamma_{\text{visc}}$ ) exerted by the host fluid is in equilibrium, i.e.,  $\Gamma_{\text{output}} = \Gamma_{\text{visc}}$ . Thereby we can retrieve  $\Gamma_{\text{output}}$  by measuring the rotation speed of the disk and calculating  $\Gamma_{\text{visc}}$  by  $\Gamma_{\text{visc}} = -(16/3)\eta R^3\Omega$  ( $\eta$  is the dynamic viscosity of air,  $R$  is the radius of the disk,  $\Omega$  is the steady angular frequency of the spinning disk). In the simulation, the acoustic radiation torque as the unique power source driving the load is utilized to characterize the torque output of the system despite slight errors caused by unknown factors (e.g., acoustic rotational streaming<sup>[17]</sup>) that are hard to precisely account for in theory. The results are plotted in Figure 4e,f, which show a controllable torque output by tuning the motor power or frequency, as well as a high rotation speed up to 1000 rpm at 4 W (see Supporting Information for details). Notice that the central frequency of 25 kHz does not refer to a theoretical peak radiation torque but a maximum proportion of the desired OAM mode, which is the reason for the slight offset between the central frequency and peak of the torque-frequency curve. This finding verifies the performance of our mechanism and MEB for high-efficiently twisting of linear momentum to OAM in a flexible way using only a single source, with significant application potential to OAM-enabled manipulation, such as in cell centrifugation.

Furthermore, to reveal the versatility and generality of our mechanism, we also perform the generation of man-made OAM with a fan-shaped MEB at an audio frequency of 3430 Hz. **Figure 5a,b** shows a photo of the audible experimental setup and 3D-printed MEB with radius  $kR = \mu_1^5$ , respectively (see Supporting Information for detailed structural parameters and acoustical properties of the metastructure unit cell for audible regime). For a clear illustration, we first measured the sound pressure distribution along the polar axis. As proved by **Figure 5c**, as expected, the theoretical first-order Bessel profile is observed in the experiment. Then we measured the 2D sound amplitude and phase distribution in a circular region and plotted the experimental results in **Figure 5d,e**. The results that show a donut-shaped profile of the amplitude and spiral phase validate the effective conversion from unidirectional linear momentum to OAM of the first order in the designed MEB. Our mechanism also applies to the production of high-order OAM modes. Take a 10th-order OAM excitation for instance, **Figure 5f,g** shows the simulated results of the normalized amplitude and phase distributions of the generated 2D vortex within another fan-shaped MEB with a judiciously modulated boundary, which exhibits the desired whole-area 2D Bessel patterns as well as the 10th-order azimuthal dependence of phase. Notice that, although the incident plane wave is realized by a line array in the experiment, the universality of our proposed mechanism also ensures in-plane OAM production for a single

emitter placed either in the far-field mimicking a plane wave, or in the near-field with different wavevector components given that the MEB's boundary has been modulated based on our derived generalized formulae. Besides, it is also apparent that our mechanism enables integrating multiple MEBs into one 2D single-source system, which may be of great significance for OAM multiplexing and OAM-based communication.<sup>[46]</sup> Moreover, given that our theoretically derived criterion ( $kR = \mu_m^i$ ) is frequency-dependent, by simply changing the driving frequency our mechanism can further enable switching between different OAM states inside a specific MEB, which in practice can be implemented using a broadband metastructure.<sup>[47,48]</sup>

### 3. Conclusion

We have designed a compact and arbitrarily shaped ultrasonic motor built with an MEB that twists linear to OAM in a single-source 2D system. Thanks to a theoretically derived criterion, such twisting in the MEB is made possible by modulating its boundaries. The performance of the designed acoustic motor is demonstrated through several distinct examples of generating in-plane OAM and contactless rotation of sound-absorbing objects. The simulated and experimental results exhibit the highly efficient momentum twisting inside MEB regardless of geometrical irregularities and the source number. We anticipate that our MEB-based acoustic motor, which uses only one single source, operates at arbitrary MEB geometries, and deeply simplify the configuration can offer new possibilities for wave manipulation in 2D acoustical systems. Further, such a simple contactless engine may have far-reaching implications in various on-chip applications such as chip-scale encoding/decoding and noninvasive micro-particle manipulation.

### 4. Experimental Section

The part  $S_1$  and the rigid boundary part of MEB were fabricated with high-precision 3D printing technology (nanoArch S140, 10  $\mu\text{m}$  in precision) using photosensitive resin and a numerical control machine using aluminum alloy 6061, respectively. The rotation speed of the foam disk was measured using a laser velocimeter. The sound fields in Figure 5d,e were measured using two 1/4-in. microphones (Brüel & Kjær type-4961) with one scanning the target region inside the fan-shaped MEB point by point, and another one fixed outside as a reference signal. By using the software PULSE Labshop, the cross-spectrum of the two signals was obtained and thereby retrieve the sound phase and amplitude. The measurements of sound field scanning were taken at every  $\pi/12$  in the azimuthal and every 1 cm in the radial direction.

### Supporting Information

Supporting Information is available from the Wiley Online Library or from the author.

### Acknowledgements

The authors would like to thank Prof. Tao Li for fruitful discussions. This work was supported by National Key R&D Program of China (Grant No. 2017YFA0303700), the National Natural Science Foundation of China

(Grant Nos. 11634006, 11374157, and 81127901), a project funded by the Priority Academic Program Development of Jiangsu Higher Education Institutions and High-Performance Computing Center of Collaborative Innovation Center of Advanced Microstructures. J.C. acknowledges the support from the European Research Council (ERC) through the Starting Grant No. 714577 PHONOMETA.

### Conflict of Interest

The authors declare no conflict of interest.

### Author Contributions

J.L., B.L., and J.C. conceived the idea and designed the experiment. J.L., Z.L., Y.D., and A.C. prepared the samples and performed the experiment. J.L. conducted numerical simulations. J.L., B.L., J.C., and J.-J.C. contributed to the writing of the paper. B.L., J.C., and J.-J.C. supervised the entire study.

### Data Availability Statement

The data that support the findings of this study are available from the corresponding author upon reasonable request.

### Keywords

contactless rotation, meta engine blocks, momentum twisting, ultrasonic motors

Received: February 17, 2022

Revised: March 31, 2022

Published online: June 9, 2022

- [1] M. Fatemi, J. F. Greenleaf, *Science* **1998**, *280*, 82.
- [2] M. X. Lim, A. Souslov, V. Vitelli, H. M. Jaeger, *Nat. Phys.* **2019**, *15*, 460.
- [3] K. Dholakia, B. W. Drinkwater, M. Ritsch-Martens, *Nat. Rev. Phys.* **2020**, *2*, 480.
- [4] J. Friend, L. Y. Yeo, *Rev. Mod. Phys.* **2011**, *83*, 647.
- [5] M. Padgett, R. Bowman, *Nat. Photonics* **2011**, *5*, 343.
- [6] A. Marzo, B. W. Drinkwater, *Proc. Natl. Acad. Sci. USA* **2019**, *116*, 84.
- [7] W. C. Lo, C. H. Fan, Y. J. Ho, C. W. Lin, C. K. Yeh, *Proc. Natl. Acad. Sci. USA* **2021**, *118*, e2023188118.
- [8] Z. Tian, Z. Wang, P. Zhang, T. D. Naquin, J. Mai, Y. Wu, S. Yang, Y. Gu, H. Bachman, Y. Liang, Z. Yu, T. J. Huang, *Sci. Adv.* **2020**, *6*, eabb0494.
- [9] Y. Yang, T. Ma, S. Li, Q. Zhang, J. Huang, Y. Liu, J. Zhuang, Y. Li, X. Du, L. Niu, Y. Xiao, C. Wang, F. Cai, H. Zheng, *Research* **2021**, *2021*, 9781394.
- [10] Y. Y. Tanaka, P. Albella, M. Rahmani, V. Giannini, S. A. Maier, T. Shimura, *Sci. Adv.* **2020**, *6*, eabc3726.
- [11] A. Ozcelik, J. Rufo, F. Guo, Y. Gu, P. Li, J. Lata, T. J. Huang, *Nat. Methods* **2018**, *15*, 1021.
- [12] B. T. Hefner, P. L. Marston, *J. Acoust. Soc. Am.* **1999**, *106*, 3313.
- [13] A. Marzo, S. A. Seah, B. W. Drinkwater, D. R. Sahoo, B. Long, S. Subramanian, *Nat. Commun.* **2015**, *6*, 8661.
- [14] K. Volke-Sepúlveda, A. O. Santillán, R. R. Boullosa, *Phys. Rev. Lett.* **2008**, *100*, 024302.
- [15] L. Zhang, P. L. Marston, *Phys. Rev. E* **2011**, *84*, 065601.

- [16] M. A. Ghanem, A. D. Maxwell, Y. N. Wang, B. W. Cunitz, V. A. Khokhlova, O. A. Sapozhnikov, M. R. Bailey, *Proc. Natl. Acad. Sci. USA* **2020**, *117*, 16848.
- [17] A. Anhäuser, R. Wunenburger, E. Brasselet, *Phys. Rev. Lett.* **2012**, *109*, 034301.
- [18] C. E. M. Demore, Z. Yang, A. Volovick, S. Cochran, M. P. MacDonald, G. C. Spalding, *Phys. Rev. Lett.* **2012**, *108*, 194301.
- [19] D. Foresti, D. Poulidakos, *Phys. Rev. Lett.* **2014**, *114*, 024301.
- [20] Z. Tian, S. Yang, P.-H. Huang, Z. Wang, P. Zhang, Y. Gu, H. Bachman, C. Chen, M. Wu, Y. Xie, T. J. Huang, *Sci. Adv.* **2019**, *5*, eaau6062.
- [21] X. Jiang, Y. Li, B. Liang, J. C. Cheng, L. Zhang, *Phys. Rev. Lett.* **2016**, *117*, 034301.
- [22] M. Baudoin, J.-C. Gerbedoen, A. Riaud, O. B. Matar, N. Smagin, J.-L. Thomas, *Sci. Adv.* **2019**, *5*, eaav1967.
- [23] C. Chen, Y. Gu, J. Philippe, P. Zhang, H. Bachman, J. Zhang, J. Mai, J. Rufo, J. F. Rawls, E. E. Davis, N. Katsanis, T. J. Huang, *Nat. Commun.* **2021**, *12*, 1118.
- [24] S. Gspan, A. Meyer, S. Bernet, M. Ritsch-Marte, *J. Acoust. Soc. Am.* **2004**, *115*, 1142.
- [25] E. Karimi, S. A. Schulz, I. D. Leon, H. Qassim, J. Upham, R. W. Boyd, *Light: Sci. Appl.* **2014**, *3*, e167.
- [26] X. Jiang, B. Liang, J. C. Cheng, C. W. Qiu, *Adv. Mater.* **2018**, *30*, 1800257.
- [27] X. Jiang, J. Zhao, S.-l. Liu, B. Liang, X.-y. Zou, J. Yang, C.-W. Qiu, J.-c. Cheng, *Appl. Phys. Lett.* **2016**, *108*, 203501.
- [28] Z. Hong, J. Zhang, B. W. Drinkwater, *Phys. Rev. Lett.* **2015**, *114*, 214301.
- [29] C. R. P. Courtney, B. W. Drinkwater, C. E. M. Demore, S. Cochran, A. Grinenko, P. D. Wilcox, *Appl. Phys. Lett.* **2013**, *102*, 123508.
- [30] J. J. Liu, B. Liang, J. C. Cheng, *Phys. Rev. Appl.* **2021**, *15*, 014015.
- [31] H.-Z. Chen, T. Liu, H.-Y. Luan, R.-J. Liu, X.-Y. Wang, X.-F. Zhu, Y.-B. Li, Z.-M. Gu, S.-J. Liang, H. Gao, L. Lu, L. Ge, S. Zhang, J. Zhu, R.-M. Ma, *Nat. Phys.* **2020**, *16*, 571.
- [32] P. Miao, Z. Zhang, J. Sun, W. Walasik, S. Longhi, N. M. Litchinitser, L. Feng, *Science* **2016**, *353*, 464.
- [33] J. Ni, C. Huang, L. M. Zhou, M. Gu, Q. Song, Y. Kivshar, C. W. Qiu, *Science* **2021**, *374*, eabj0039.
- [34] X. Cai, J. Wang, M. J. Strain, B. Johnson-Morris, J. Zhu, M. Sorel, J. L. O'Brien, M. G. Thompson, S. Yu, *Science* **2012**, *338*, 363.
- [35] J. Lu, C. Qiu, M. Ke, Z. Liu, *Phys. Rev. Lett.* **2016**, *116*, 093901.
- [36] B. Assouar, B. Liang, Y. Wu, Y. Li, J.-C. Cheng, Y. Jing, *Nat. Rev. Mater.* **2018**, *3*, 460.
- [37] Y. Xie, W. Wang, H. Chen, A. Konneker, B. I. Popa, S. A. Cummer, *Nat. Commun.* **2014**, *5*, 5553.
- [38] X. Zhu, K. Li, P. Zhang, J. Zhu, J. Zhang, C. Tian, S. Liu, *Nat. Commun.* **2016**, *7*, 11731.
- [39] Y. Li, X. Jiang, B. Liang, J. Cheng, L. Zhang, *Phys. Rev. Appl.* **2015**, *4*, 024003.
- [40] Y. Jin, R. Kumar, O. Poncelet, O. Mondain-Monval, T. Brunet, *Nat. Commun.* **2019**, *10*, 143.
- [41] T. Brunet, J. Leng, O. Mondain-Monval, *Science* **2013**, *342*, 323.
- [42] C. R. P. Courtney, C.-K. Ong, B. W. Drinkwater, A. L. Bernassau, P. D. Wilcox, D. R. S. Cumming, *Proc. R. Soc. A* **2012**, *468*, 337.
- [43] X. Ding, S.-C. S. Lin, B. Kiraly, H. Yue, S. Li, I.-K. Chiang, J. Shi, S. J. Benkovic, T. J. Huang, *Proc. Natl. Acad. Sci. USA* **2012**, *109*, 11105.
- [44] J. Christensen, A. I. Fernandez-Dominguez, F. de Leon-Perez, L. Martin-Moreno, F. J. Garcia-Vidal, *Nat. Phys.* **2007**, *3*, 851.
- [45] W. Y. Tsai, Q. Sun, G. Hu, P. C. Wu, R. J. Lin, C. W. Qiu, K. Ueno, H. Misawa, D. P. Tsai, *Adv. Opt. Mater.* **2019**, *7*, 1801060.
- [46] T. Lei, M. Zhang, Y. Li, P. Jia, G. N. Liu, X. Xu, Z. Li, C. Min, J. Lin, C. Yu, H. Niu, X. Yuan, *Light: Sci. Appl.* **2015**, *4*, e257.
- [47] K. Li, B. Liang, J. Yang, J. Yang, J.-C. Cheng, *Appl. Phys. Express* **2018**, *11*, 077301.
- [48] R.-Q. Li, B. Liang, Y. Li, W.-W. Kan, X.-Y. Zou, J.-C. Cheng, *Appl. Phys. Lett.* **2012**, *101*, 263502.